Post-print of S. Signetti et al., *J. Phys. D: Appl. Phys.*, **52** (2019) 255305. DOI: 10.1088/1361-6463/ab1581

A numerical-experimental approach towards picomechanics and picotribology: the case study of defective carbon nanotubes bundles

Stefano Signetti,[1, a)] Xiaoming Chen,[2, b)] Changhong Ke,[2] and Nicola M. Pugno[1, 3, 4, c)]
[1)] *Laboratory of Bio-Inspired and Graphene Nanomechanics, Department of Civil, Environmental and Mechanical Engineering, University of Trento, Trento, Italy*
[2)] *Department of Mechanical Engineering, State University of New York at Binghamton, Binghamton, NY, United States of America*
[3)] *School of Engineering and Materials Science, Queen Mary University of London, London, United Kingdom*
[4)] *Ket-Lab, Edoardo Amaldi Foundation, Roma, Italy*

We present a simulation study on the peeling of carbon nanotubes bundles interacting with a flat substrate, represented by the back surface of an atomic force microscopy cantilever. A defected sample, acquired *in situ* using a scanning electron microscope, was investigated under different peeling configurations by finite element method simulations. The coupled computational-experimental analysis let to identify the position and the entity of a structural defect by means of reverse image correlation problem. By exploiting this defective fibre it was also possible to quantify, as indirect measure, the friction and adhesion forces between the bundle and the substrate of few pN magnitude, otherwise difficult to measure with the resolution of currently available instruments. The proposed approach can be useful to study the tribology-induced mechanical behaviour of one-dimensional nanostructures as well as for real-time identification and monitoring of nanodefects for industrial applications, such as nanoelectronics.

Keywords: Peeling experiments, Carbon nanotubes bundle, Friction, Adhesion, Defect identification, Finite element simulation

I. INTRODUCTION

One dimensional (1D) nanostructures, such as carbon nanotubes (CNTs)[1–3], possess outstanding mechanical, electrical, chemical and thermal properties making them ideal for their use in multifunctional advanced composites for electronics, sensors, filters, and biomedicine. Due to their large surface-volume ratio, interface interactions play a fundamental role in their mechanical and functional properties, and dynamics. Adhesion properties of such bundles with various substrates have been extensively investigated via combined theoretical-experimental-computational approaches[4–16]. Prior studies have revealed that CNTs may possess a variety of structural defects, e.g. Stone–Wales transformations[17], which are generated during either synthesis or post-processing stages and substantially affect their structural and mechanical properties[18–20]. The adhesion between nanotubes and substrates combined with their slenderness may lead into severe transverse and buckling deformations[21], possibly amplified by the presence of such defects. This may impact their applications, such as the performance of THz antennas[22] or of nano heat pipes for electronic systems[23]. Therefore, it is of paramount importance to understand the role of material and geometrical nonlinearities and to study the actual CNTs behaviour in non-ideal configurations which, however, remains largely unexplored.

The difficulties in studying such systems are due to the technical challenge in the simultaneous high-resolution measurement of the peeling deformation of microscale interacting structures and the corresponding peeling force of few pN with adequate spatial and force resolutions. These are mainly limited by capabilities of currently available experimental measurement devices and the mismatch between the size scale of the manipulated object and the characteristic scale of interacting surfaces. Indeed, such measurements have been reported so far by few research groups in the world[14]. Computational atomistic modeling has been also used to describe the adhesive behaviour of carbon nanotubes over various substrates[14,16], but while it is suitable to understand the origin and nature of adhesive interactions, it cannot be used to directly correlate the effect of tribological interaction to the microscopic deformation of the bundle alone or within a more complex architecture. Such models are also relatively time consuming, limited in the size and time scales of the system that can be modeled, and cannot be exploited for image correlation techniques on microscopic samples. Continuum analytical and finite element method (FEM) models have been extensively used to model the bending, peeling, and buckling behaviour of such nanostructures[21,24] but, to the best of authors' knowledge, there are no specific exploitation for indirect defect characterization and estimation of tribological properties.

In this paper we present a coupled computational-

[a)] SS currently at: Department of Mechanical Engineering, Korea Advanced Institute of Science and Technology (KAIST), Daejeon, Republic of Korea
[b)] XC currently at: Micro- and Nanotechnology Research Center, State Key Laboratory for Manufacturing Systems Engineering, Xi'an Jiaotong University, Xi'an, People's Republic of China
[c)] Electronic mail: nicola.pugno@unitn.it

experimental approach to derive the structural and tribological properties of a defective CNTs bundle. The procedure was successfully used to interpret the results of a prior peeling study[25] on the same bundle interacting with a flat substrate represented by the back surface of an atomic force microscopy (AFM) cantilever probe inside a scanning electron microscope (SEM). Thanks to finite element method (FEM) simulations and exploiting the defective nature of the bundle, we were able derive information on the tribological properties of the bundle, which consist of few-pN magnitude forces, otherwise difficult to be directly measured due to the resolution limits of current instrumentation. The proposed model and algorithm may be useful to study the tribology-induced mechanical behaviour of 1D nanostructures as well as for real-time identification and monitoring, via machine vision systems[26,27], of defects in nanofibres for industrial applications.

II. MATERIALS AND METHODS

A. In situ SEM geometry acquisition and nanomechanical peeling experiments

The CNTs fibre used in this study was prepared by using chemical vapor deposition (CVD) synthesized single-walled CNTs that were original grown on a silicon wafer. Thin-bundled CNTs were formed when they were transferred to copper transmission electron microscope (TEM) grids. Prior characterization by high resolution transmission electron microscopy (HRTEM)[24,28] has shown that these thin CNTs fibres are composed of parallel and tightly bound individual CNTs.

The adopted experimental setup is illustrated in Figure 1(a). The nanomechanical peeling measurements were performed *in situ* inside a high resolution SEM (FEI Nanolab 600)[29]. The tested CNTs fibre was mounted on a nanomanipulator, used for moving it in various peeling configurations. Electron beam induced deposition (EBID) of carbon was used to enhance the attachment of the CNTs fibre to the nanomanipulation probe. Silicon AFM cantilevers (CSG 01, NT-MDT) with a 5 nm gold (Au) coating on their back surfaces were employed and mounted vertically on the SEM stage. The AFM cantilevers have a nominal spring constant of 0.03 N/m and a width of 30 µm. The spring constant of each employed AFM cantilevers was calibrated using thermal tuning methods. The actual spring constant of the cantilever used in this test was 0.064 N/m. However, due to the much higher elastic transverse compliance of the bundle, the deformation of the cantilever is much smaller than the deformation of the fibre and can be neglected. From the recorded high resolution SEM images, the overall length of the CNTs fibre ($\overline{\mathrm{AB}}$) was measured to be about 28.05 µm, while the length from the control point on the manipulator and the right-side free end (segment $\overline{\mathrm{OB}}$) was of 20.50 µm. These quantities were verified from various experimental images reproducing other deformed states[25] (see Supplementary Figure S1), thus excluding tilt artifacts.

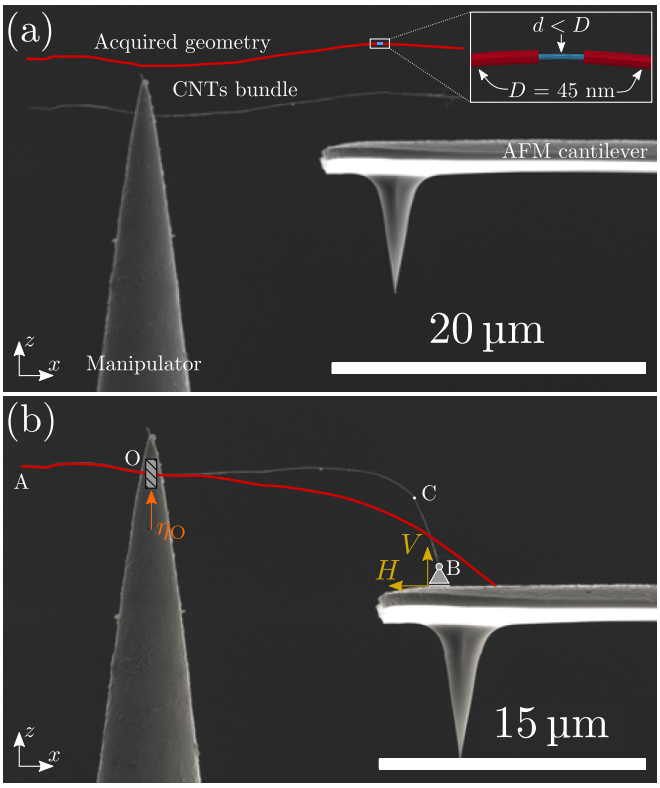

FIG. 1. (a) SEM image used for the acquisition of the reference geometry of the bundle (undeformed state) and detail of the FEM model at the defect location. (b) The experimental final position of the bundle after peeling is depicted with the static scheme adopted in FEM simulations. The red line is the simulation-derived deformed shape without the presence of the defect ($d = D = 45$ nm) and assumption of no friction force ($H = 0$) at the contact point with the AFM cantilever. *In situ* SEM images reproduced with permission from Ref.[25].

The geometry of the fibre was acquired via a CAD software from the *in situ* SEM images. A slope discontinuity in the elastica was observed in the pull-out AFM experiments (point C), confirming that the peeling configuration was not compatible with the deformation of a defect-free structure, thus suggesting the presence of a structural imperfection (Figure 1(b)). The position of the defect along the bundle was identified by analyzing the first derivative of the piecewise function $f(x)$ which describes the geometry of the fibre and corresponds to the maximum jump in the slope function $f'(x) = \frac{\mathrm{d}f}{\mathrm{d}x}$ in the deformed part of the fibre (see Figure S2 in the Supplementary Material for details).

B. FEM model and computational procedure

The acquired geometry from the SEM images was sampled with segments of length l=75 nm, overall resulting in 374 beam elements. The same discretization, which ensured a sufficiently smooth line, was used also for the numerical model in order to have the same nodal coordinates for image correlation technique. The element formulation used in the model is a Hughes-Liu formulation[30] which is suitable for such low aspect ratios (l/D=1.6:1). Such discretization was demonstrated to ensure convergence in terms of deformed shape and peeling forces in various configurations[25]. An implicit scheme was used for solving the model (total simulated time 4 s, timestep Δt= 10 ms). According to our previous measurements on similar bundles[21], the cross-section was assumed circular with diameter D=45 nm and the Young's modulus E = 197 GPa. The defect was modeled with a reduced cross-section with $d < D$ for two beam elements adjacent to the node identified as defect location (Figure 1(a)). Thus, the simulated length of the defect was $l_{\text{def}} = 150$ nm, and can be considered as punctual if compared to the overall bundle length.

Figure 1(b) shows the geometry of the bundle after peeling experiment together with the structural scheme adopted in the numerical simulations. The bundle is fully clamped to the probe (point O) and no relative displacements and rotations are allowed there. The probe is moved up of an imposed displacement η_{O}= [0, 0, 7.43] µm, determined from image acquisitions (the sign of displacements refers to the positive direction of coordinate axes, see Supplementary Figure S1 and Video S1 for the sequence of the entire peeling process). The restraint at contact point with the AFM (point B) was modeled as a horizontal slider. In addition to the vertical force V that arises at the restrain, namely adhesion, an horizontal force H was introduced at this stage to simulate friction that prevents the elastic return of the bundle causing the experimentally observed deformed shape, which would be otherwise impossible to obtain with just the vertical reaction, as can be seen from the simulation depicted in Figure 1(b) with $H = 0$.

To determine the magnitude of the contact forces and the entity of the structural defect, the carried analysis aimed at minimizing the average nodal distance m between the deformed geometry obtained from FEM simulations and experiments in the final equilibrium configuration. Thus, the estimate of the defect diameter was obtained as follows:

$$d^* = \arg\min \left\{ \frac{m}{D} = \frac{1}{ND} \sum_{i=1}^{N} \sqrt{{\Delta x_i}^2 + {\Delta z_i}^2} \right\} \qquad (1)$$

where $N = 273$ is the number of nodes used to sample the portion of the bundle actually subjected to deformation (segment $\overline{OB}$), Δx_i and Δz_i are the differences between the components of the FEM computed and the experimental coordinates of each node. The out-of-plane (y direction) displacements were neglected because of the high-precision control of the probe, which resulted in no measurable difference in bundle length between peeling and rest configuration. The procedure adopted in the simulation to compute the defect entity and of interaction forces was based on the following steps:

1. a tentative cross-section diameter $d \leq 45$ nm is assumed at the determined defect site;
2. the value of H that makes the experimental and simulation coordinates of point B at peeling equilibrium to overlap (tolerance of ±5 nm) is computed iteratively;
3. the corresponding vertical reaction V at point B and the normalized deviation m/D are computed for the identified equilibrium configuration;
4. the procedure 1-3 is repeated for different values of $d \leq D$, until a minimum of the parameter m/D is found and the corresponding reduced cross-section diameter d^* (Equation (1)) is assumed as an estimate of the defect entity.

Note that the whole procedure could be easily automatized, as schematized in the flow chart of Supplementary Figure S3 to allow a real-time identification of defect and interface forces. The procedure may be extended also to the case of multiple defects, which would reflect in a larger investigation domain and number of iterations.

III. RESULTS AND DISCUSSION

A. Determination of defect entity and tribological properties

In Table I the different tested cases are presented, indicating for each the defect size, the values of the reaction forces at the bundle tip and of the minimization parameter m/D. We conclude that the defect has an equivalent diameter $d^* \approx 18$ nm, which resulted in a good superposition between the simulated and experimental deformed geometry (Figure 2(a)) and it is compatible with commonly recorded defects in such CNTs structures[18–20]. The comparison for all cases is reported in the Supplementary Figures S4-S16, and Video S1 shows the simulation with $d = d^*$.

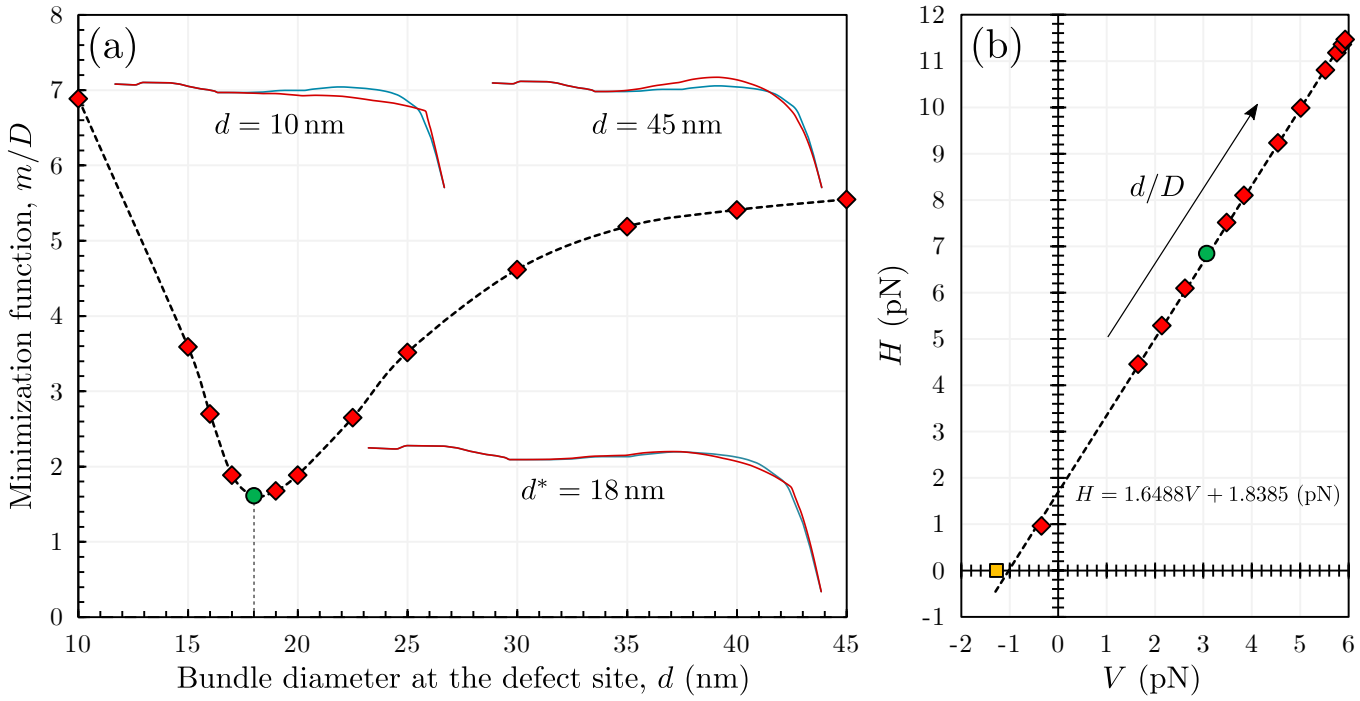

FIG. 2. (a) Evolution of the normalized residual m/D at the equilibrium peeling configuration for different values of d. The minimum corresponds to an estimated defect diameter $d^* \approx 18\,\text{nm}$. Three limit configurations are depicted, superimposing simulations to experiment. (b) Derived friction law and corresponding parameters from the best-fit of the $H - V$ results from FEM simulations (Table I). The yellow point corresponds to the simulated case with $H = 0$ and $d = 45\,\text{nm}$ (Figure 1(b)) and it is not included in the fit.

TABLE I. Residual function m/D, friction and adhesion forces as computed from the different simulated cases (d/D). The sign of the forces refers to directions depicted in Figure 1(b).

d (nm)	d/D	H (pN)	V (pN)	m/D
10.0	0.222	0.96	-0.35	6.89
15.0	0.333	4.45	1.65	3.59
16.0	0.356	5.29	2.14	2.70
17.0	0.378	6.09	2.62	1.89
18.0	0.400	6.84	3.07	1.61
19.0	0.422	7.51	3.48	1.68
20.0	0.444	8.10	3.84	1.89
22.5	0.500	9.23	4.54	2.65
25.0	0.556	9.98	5.01	3.52
30.0	0.667	10.80	5.52	4.62
35.0	0.778	11.18	5.76	5.19
40.0	0.889	11.36	5.87	5.41
45.0	1.000	11.46	5.93	5.55

Furthermore, we exploited all the performed simulations to determine the friction and adhesion at the contact point. Assuming the interaction in the form of a generalized Coulomb's friction law as $H = \mu\, V + \Gamma$[31] the friction coefficient μ and the adhesion force Γ can be determined by linear fit on the computed points (H_i, V_i). From our simulations we computed $\mu \approx 1.65$ and $\Gamma \approx 1.84\,\text{pN}$. The computed adhesion is $\gamma = \Gamma/D \approx 41\,\mu\text{N/m}$, which is compatible with literature values among various substrates[15]. Apart from the case of $d = 10\,\text{nm}$, for compatibility conditions the bundle is always compressed and for $d^* = 18\,\text{nm}$ the resultant compressive axial force is lower than 7.5 pN, while the maximum bending moment occurs in the proximity of the defect section and it is equal to $3 \cdot 10^{-5}$ pNm (Supplementary Figure S17). Although the bundle was free to move along y, negligible movement was recorded in the out-of-plane direction from our simulations. To evaluate possible artifacts in the acquisition of the geometry and related estimation of contact forces, we evaluated the effects of a lateral movement of the probe. In addition to the previous configuration we applied a lateral displacement $\eta_O = [0, 2.89, 0]\,\mu\text{m}$ to the bundle with $d = d^*$: this would reflect to a maximum difference of 1 % in the projected length of the bundle on the xz plane. In this limit configuration we calculated $H = 6.45\,\text{pN}$ and $V = 2.75\,\text{pN}$, which are slightly lower than the previously computed values (Table I). Assuming these values as lower bounds of the real reactions, the uncertainty on the estimate would be $H = 6.64 \pm 0.19\,\text{pN}$ and $V = 2.91 \pm 0.16\,\text{pN}$. Thus, even a relatively poor control of the probe would not significantly affect the estimation of contact interactions, confirming results on our previous peeling experiments[25].

B. Buckling experiment and analysis

In a second configuration, the analyzed CNTs bundle experienced buckling deformation when approaching to the AFM back surface. This conclusion is supported by the geometry acquisition (Figure 3(a)), which provided a projected length of only 24.9 µm, somewhat lower with respect to the actual length of the bundle of 28.05 µm measured both at the rest (Figure 1(a)) and in the peeling configuration (Figure 1(b)) previously presented. This hypotesis implies an out-of-plane (y direction) displacement of the fibre, which is confirmed by the fact that the final part of the bundle is not at the same focusing length under the SEM electron beam. Given that, it was not possible to quantitatively apply the inverse approach proposed above, since the exact coordinates (y components) were not known, but some considerations on the system could be made anyway.

To derive more information about the interactions generating the buckling deformation, a further set of simulations was performed in order to determine the components of the force $\vec{P}$ acting on the bundle tip. This concentrated buckling force is considered as the resultant of a distributed load which likely occurs on the bundle due to the electron beam induced charge accumulation on the AFM and on the bundle[32,33]. We first computed the x and z components of the tip displacement (point B) as difference between the known initial and final post-buckling configuration being respectively at $x_\mathrm{B} = -4.09\,\mu\mathrm{m}$ and $z_\mathrm{B} = -0.16\,\mu\mathrm{m}$. These two determined components were imposed to the tip while the third one, y_B, was varied to minimize the difference between the simulated and experimental projection of the deformed bundle on the vertical plane. The simulation obtained deformed shape, based upon the defective bundle determined from our previous calculations, is qualitatively consistent with the one obtained from experiments (Figure 3(a) and Supplementary Video S2). A localized rotation at the defect location is clearly visible, providing a further proof of its actual presence. The magnitude of the components of $\vec{P}$ that cause the buckling configuration were determined at equilibrium, being equal to $P_\mathrm{x} = 9.83\,\mathrm{pN}$, $P_\mathrm{y} \approx 3.91\,\mathrm{pN}$, $P_\mathrm{z} = 0.77\,\mathrm{pN}$ (Figure 3(b), refer to Figure 3(a) for direction).

The component of $\vec{P}$ along the bundle longitudinal axis can be derived by studying the stability of an equivalent 2 degrees-of-freedom (2DOFs) system (Figure 4), comprised of two rigid bars of length $l_1 = \overline{\mathrm{OC}} = 15.25\,\mu\mathrm{m}$ and $l_2 = \overline{\mathrm{CB}} = 5.25\,\mu\mathrm{m}$ and subjected to the axial load P. The bending stiffness of the segment $\overline{\mathrm{OC}}$ is taken into account by the rotational spring at point O with $k_1 = 3EI/l_1$, where $I = \pi D^4/64$ is the bundle cross-section moment of inertia. The defect and the deformation of the segment $\overline{\mathrm{CB}}$ are taken into account by the rotational spring at point C with $k_2 = E/\left(\frac{l_\mathrm{def}}{I^*} + \frac{l_2}{3I}\right)$, where $I^* = \pi d^{*4}/64$. The displacements in the plane of instability η_C and η_B of the defect section and of the bundle tip, respectively, are assumed as generalized coordinates. The total potential energy W of this system (Figure 4) can be expressed as:

$$\begin{aligned} W(\eta_\mathrm{B},\eta_\mathrm{C}) =& \frac{1}{2}k_1\left(\arcsin\frac{\eta_\mathrm{C}}{l_1}\right)^2 \\ &+ \frac{1}{2}k_2\left(\arcsin\frac{\eta_\mathrm{C}}{l_1} - \arcsin\frac{\eta_\mathrm{B}-\eta_\mathrm{C}}{l_2}\right)^2 \\ &- P\left\{l_1\left[1-\cos\left(\arcsin\frac{\eta_\mathrm{C}}{l_1}\right)\right]\right. \\ &\left.+ l_2\left[1-\cos\left(\arcsin\frac{\eta_\mathrm{B}-\eta_\mathrm{C}}{l_2}\right)\right]\right. . \end{aligned} \tag{2}$$

By expanding W according to the second order Taylor's series in the nearby of the origin we obtain:

$$\begin{aligned} W(\eta_\mathrm{B},\eta_\mathrm{C}) \approx& \frac{1}{2}k_1\left(\frac{\eta_\mathrm{C}}{l_1}\right)^2 + \frac{1}{2}k_2\left(\frac{\eta_\mathrm{C}}{l_1} - \frac{\eta_\mathrm{B}-\eta_\mathrm{C}}{l_2}\right)^2 \\ &- \frac{1}{2}P\left[\frac{{\eta_\mathrm{C}}^2}{l_1} + \frac{(\eta_\mathrm{B}-\eta_\mathrm{C})^2}{l_2}\right]. \end{aligned} \tag{3}$$

The equilibrium condition can be found by imposing the stationariness of the potential, i.e. $\frac{\partial W}{\partial \eta_i} = 0$, which yields to the following homogeneous linear system of algebraic equations:

$$[W']\,(\eta) = \begin{bmatrix} w_{11} & w_{12} \\ w_{21} & w_{22} \end{bmatrix}\begin{pmatrix} \eta_\mathrm{C} \\ \eta_\mathrm{B} \end{pmatrix} = \begin{pmatrix} 0 \\ 0 \end{pmatrix} \tag{4}$$

where

$$w_{11} = -P\left(\frac{1}{l_1}+\frac{1}{l_2}\right) + \frac{k_1}{l_1^2} + k_2\left(\frac{1}{l_1^2}+\frac{2}{l_1 l_2}+\frac{1}{l_2^2}\right) \tag{5a}$$

$$w_{12} = w_{21} = \frac{P}{l_2} - k_2\left(\frac{1}{l_1 l_2}+\frac{1}{l_2^2}\right) \tag{5b}$$

$$w_{22} = -\frac{P}{l_2} + \frac{k_2}{l_2^2} \tag{5c}$$

The system admits a non-trivial solution when $\det[W'] = 0$, from which it is possible to determine the first eigenvalue corresponding to the lower critical buckling load:

$$\begin{aligned} P_\mathrm{crit} =& \frac{1}{2}\left\{\frac{k_1}{l_1} + k_2\left(\frac{1}{l_1}+\frac{1}{l_2}\right)\right. \\ &\left. - \sqrt{\left[\frac{k_1}{l_1} + k_2\left(\frac{1}{l_1}+\frac{1}{l_2}\right)\right]^2 - \frac{4k_1k_2}{l_1l_2}}\right\} \end{aligned} \tag{6}$$

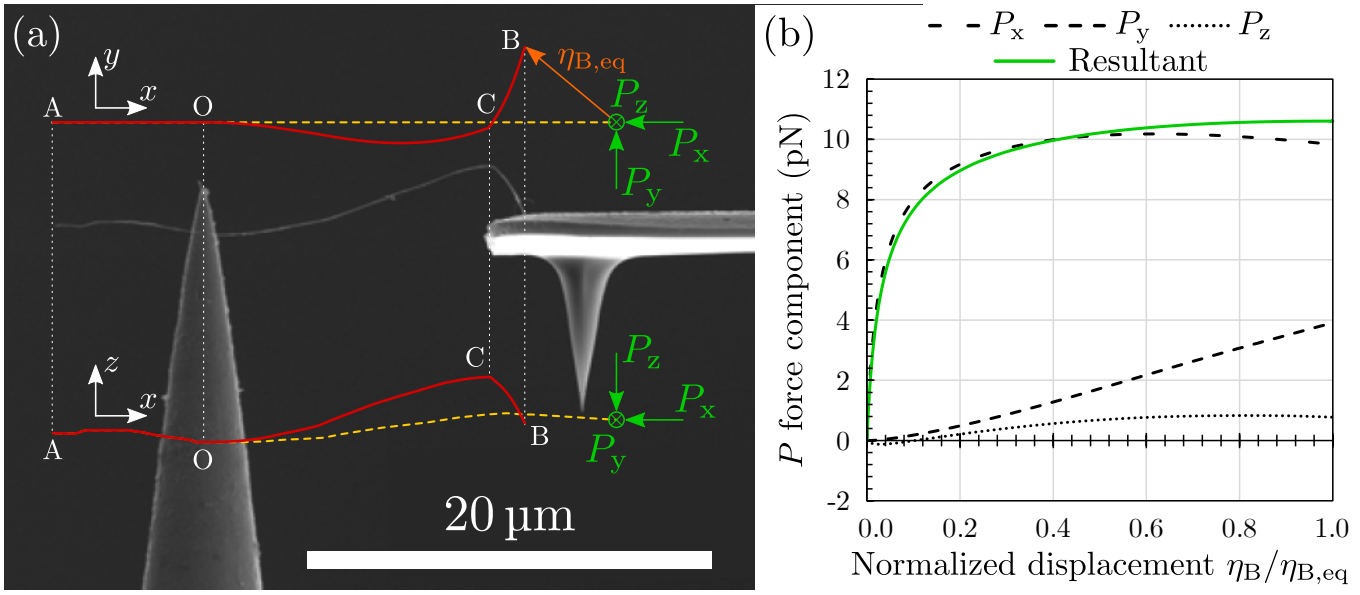

FIG. 3. (a) SEM image (lateral view) of the buckled CNTs bundle compared with the simulation derived deformed shape (in red, lateral xz and top xy views) obtained with the estimated defect size (see Supplementary Videos S2-S3 for simulation animations). The yellow dashed line depicts the initial configuration of the bundle. (b) Evolution of the three component and the resultant of $\vec{P}$ during the buckling simulation vs. the corresponding normalized displacement of point B.

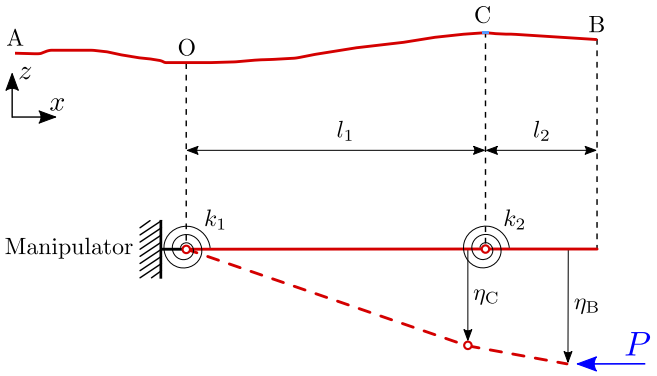

FIG. 4. 2DOFs model for the buckling analysis of the bundle.

which returns $P_{crit} = 33.6\,\text{pN}$. This value represents an upper bound since it was obtained neglecting the contemporary action of the y component of P and of further geometrical imperfections of the bundle, and under the assumption of rigid elements with concentrated elasticity and in-plane buckling. By substituting Equation (6) into either of the two of Equations (4) the corresponding eigenvector is $\eta_C \approx 0.66 \cdot \eta_B$ which is in good agreement with the deformed shape at equilibrium obtained from FEM simulation (Figure 3(a)).

The observed movement of the CNTs bundle extremity is fully compatible and explained with the charge concentration caused by the curvature radius at the AFM edge. Since the width of the AFM probe is of 30 µm, the tip of the CNTs bundle likely fell on its surface and a larger vertical displacement of the tip is excluded. Figure 3(b) reports the force-displacement curves obtained from simulations for $\vec{P}$ and its components along the coordinate axes. The x component is related to an unstable equilibrium reached after a critical buckling force component $P_x = 10.2\,\text{pN}$, while the y component monotonically increases and its value at the end of the simulation represents the minimum force required to reach the equilibrium configuration. The path of the resultant buckling force $\vec{P}$ corresponds to a stable equilibrium configuration that, thus, can be maintained only by the presence of friction and adhesion with the substrate, since when contact occurs the difference of electrostatic potential would be annulled and the initial configuration partially or completely restored. In the end, this confirms the order of magnitude of adhesion and friction interaction forces previously determined.

IV. CONCLUSION

The computational procedure reported in this work by the analysis of the elastica of a defective CNTs bundle in various peeling configuration could be exploited for the study of tribological interactions of 1D nanostructures and their derivatives, ranging from biological molecular chains[34] and fibres to 2D CNTs buckypaper or 3D assemblies, such as hierarchical CNTs tubes[35]. These reliable measurements of contact interactions would be important for modeling complex architectures[36], whose structural properties rely on contact forces. Nanodefect identification and monitoring could be a further application of our results, also to be exploited for real-time control

via image correlation technique of the structural integrity of 1D nanostructures for nanoelectronics, and could be possibly implemented and enhanced by machine learning techniques.

ACKNOWLEDGEMENTS

NMP is supported by the European Commission under the Graphene Flagship Core 2 (WP14 "Composites", no. 785219) and the FET Proactive ("Neurofibres", no. 732344) and by the Italian Ministry of Education, University and Research (MIUR) under the "Departments of Excellence" grant L. 232/2016. CHK is supported by Air Force Office of Scientific Research - Low Density Materials program under Grant no. FA9550-15-1-0491 and by National Science Foundation under Grant no. CMMI-1537333. SS acknowledges support from the Ermenegildo Zegna Founder's Scholarship 2017–2018.

SUPPLEMENTARY DATA

Supplementary data available online at stacks.iop.org/JPhysD/52/255305/mmedia.

REFERENCES

[1] S. Ijima, Nature **354**, 56 (2016).
[2] T. Hertel, R. E. Walkup, and P. Avouris, Phys Rev B **58**, 13870 (1998).
[3] O. Gülseren, T. Yldirim, S. Ciraci, and C. Kılıç, Phys Rev B **65**, 155410 (2002).
[4] T. Tang, A. Jagota, and C.-Y. Hui, J Appl Phys **97**, 074304 (2005).
[5] N. Sasaki, A. Toyoda, H. Saitoh, N. Itamura, M. Ohyama, and K. Miura, e-J Surf Sci Nanotechnol **4**, 133 (2006).
[6] R. H. M. Ishikawa, and, N. Sasaki, and K. Miura, Appl Phys Lett **93**, 083122 (2008).
[7] D. Y. Khang, J. L. Xiao, C. Kocabas, S. MacLaren, T. Banks, H. Q. Jiang, Y. Y. G. Huang, and J. A. Rogers, Nano Lett **8**, 124 (2008).
[8] N. Sasaki, A. Toyoda, N. Itamura, and K. Miura, e-J Surf Sci Nanotechnol **6**, 72 (2008).
[9] M. C. Strus, L. Zalamea, A. Raman, R. B. Pipes, C. V. Nguyen, and E. A. Stach, Nano Lett **8**, 544 (2008).
[10] J. L. Xiao, H. Q. Jiang, D. Y. Khang, J. Wu, Y. Huang, and J. A. Rogers, J Appl Phys **104**, 033543 (2008).
[11] M. Ishikawa, R. Harada, N. Sasaki, and K. Miura, Phys Rev B **80**, 193406 (2009).
[12] M. C. Strus, C. I. Cano, R. B. Pipes, C. V. Nguyen, and A. Raman, Compos Sci Technol **69**, 1580 (2009).
[13] J. Buchoux, L. Bellon, S. MArsaudon, and J.-P. Aimé, Eur Phys J B **84**, 69 (2011).
[14] M. R. Roenbeck, X. Wei, A. M. Beese, M. Naraghi, A. Furmanchuck, J. T. Paci, G. C. Schatz, and H. D. Espinosa, ACS Nano **8**, 124 (2014).
[15] T. Li, A. Ayari, and L. Bellon, J Appl Phys **117**, 164309 (2015).
[16] M. R. Roenbeck, A. Furmanchuck, A. Zhi, J. T. Paci, X. Wei, S. T. Nguyen, G. C. Schatz, and H. D. Espinosa, Nano Lett **15**, 4504 (2015).
[17] G. G. Samsonidze, G. G. Samsonidze, and B. I. Yakobson, Comp Mater Sci **23**, 62 (2002).
[18] H. Jiang, X. Q. Feng, Y. Huang, K. C. Hwang, and P. D. Wu, Comput Method Appl M **193**, 3419 (2004).
[19] K. I. Tserpes and P. Papanikos, Compos Struct **79**, 581 (2007).
[20] G. Lee, C. Z. Wang, E. Yoon, N. Hwang, and K. M. Ho, Appl Phys Lett **92**, 043104 (2008).
[21] Q. Wei, M. Zheng, and C. H. Ke, Nanosci Nanotech Lett **2**, 308 (2010).
[22] S. A. Maksimenko, G. Y. Slepyan, A. M. Nemilentsau, and M. V. Shuba, Physica E **40**, 2360 (2008).
[23] Y. Fu, N. Nabiollahi, T. Wang, S. Wang, Z. Hu, B. Carlberg, Y. Zhang, X. Wang, and J. Liu, Nanotechnology **23**, 045304 (2012).
[24] C. H. Ke, M. Zheng, G. Zhou, W. Cui, N. Pugno, and R. N. Miles, Small **6**, 438 (2009).
[25] X. Chen, M. Zheng, Q. Wei, S. Signetti, N. M. Pugno, and C. H. Ke, J Appl Phys **119**, 154305 (2016).
[26] A. Kumar, IEEE Ind Electron **55**, 348 (2008).
[27] Y. Li and C. Zhang, SpringerPlus **5**, 765 (2016).
[28] C. H. Ke, M. Zheng, I. T. Bae, and G. Zhou, J Appl Phys **107**, 104305 (2010).
[29] C.-H. Ke, N. M. Pugno, B. Peng, and H. D. Espinosa, J Mech Phys Solids **53**, 1314 (2005).
[30] T. Belytschko, W. K. Liu, B. Moran, and K. Elkhodary, *Nonlinear Finite Elements for Continua and Structures*, 2nd ed. (John Wiley & Sons, 2013).
[31] N. M. Pugno, Q. Yin, X. Shi, and R. Capozza, Meccanica **48**, 1845 (2013).
[32] N. M. Pugno, C. H. Ke, and H. D. Espinosa, J Appl Mech **72**, 445 (2004).
[33] C. H. Ke, H. D. Espinosa, and N. M. Pugno, J Appl Mech **72**, 726 (2005).
[34] X. Shi, Y. Kong, Y. Zhao, and H. Gao, Acta Mech Sinica **21**, 249 (2005).
[35] F. Schütt, S. Signetti, H. Krüger, S. Röder, D. Smazna, S. Kaps, S. N. Gorb, Y. K. Mishra, N. M. Pugno, and R. Adelung, Nat Commun **8**, 1215 (2017).
[36] D. Durville, Comp Mech **49**, 687 (2012).